Recent progress on $MnBi_2Te_4$ epitaxial thin films as a platform for realising quantum anomalous Hall effect

Qile Li[1,2*], Sung-Kwan Mo[3], Mark T. Edmonds[1,2,4*]

[1]School of Physics and Astronomy, Monash University, Clayton, VIC, Australia

[2]ARC Centre for Future Low Energy Electronics Technologies, Monash University, Clayton, VIC, Australia

[3]Advanced Light Source, Lawrence Berkeley National Laboratory, Berkeley, CA, 94720 USA

[4]ANFF-VIC Technology Fellow, Melbourne Centre for Nanofabrication, Victorian Node of the Australian National Fabrication Facility, Clayton, VIC 3168, Australia

*Corresponding Author mark.edmonds@monash.edu, qile.li@monash.edu

Abstract

Since the first realisation of the quantum anomalous Hall effect (QAHE) in a dilute magnetic doped topological insulator thin film in 2013, the quantisation temperature has been limited to less than 1 K due to magnetic disorder in dilute magnetic systems. With magnetic moments ordered into the crystal lattice, the intrinsic magnetic topological insulator $MnBi_2Te_4$ has the potential to eliminate or significantly reduce magnetic disorder, and improve the quantisation temperature. Surprisingly, to date, the QAHE has yet to be observed in molecular beam epitaxy (MBE)-grown $MnBi_2Te_4$ thin films at zero magnetic field, and what leads to the difficulty in quantisation is still an active research area. Although bulk $MnBi_2Te_4$ and exfoliated flakes have been well studied, revealing both the QAHE and axion insulator phases, experimental progress on MBE thin films has been slower. Understanding how the breakdown of QAHE occurs in $MnBi_2Te_4$ thin films and finding solutions that will enable mass-produced millimetre-size QAHE devices operating at elevated temperatures is required. In this mini-review, we will summarise recent studies on the electronic and magnetic properties of MBE $MnBi_2Te_4$ thin films and discuss mechanisms that could explain the failure of QAHE from the aspects of defects, electronic structure, magnetic order, and consequences of their delicate interplay. Finally, we propose several strategies for realising QAHE at elevated temperatures in $MnBi_2Te_4$ thin films.

Introduction

Recent discovery of topological materials has led to significant scientific progress on the understanding of quantum phases of matters, such as the quantum spin Hall effect[1, 2] and quantum anomalous Hall effect (QAHE)[3-7]. These quantum phases of matter feature unique spin-momentum locked topological edge states[8, 9] which can be used for engineering dissipationless electronics[10] and novel topological superconductors with potential for fault-tolerant quantum computing applications[11]. To date, thanks to the discovery of intrinsic magnetic topological insulators - $MnBi_2Te_4$ family[12], the QAHE quantisation temperature has been improved to 1.4 K[13], well above the temperature of 30 mK where the QAHE was first realised in Cr doped $(Bi, Sb)_2Te_3$[3]. In principle, the intrinsically ordered magnetic moments in

MnBi$_2$Te$_4$ minimise the adverse effects of magnetic disorder on QAHE edge channels, thus the QAHE should only be limited by the magnetic transition temperature of the materials and the size of the Dirac gap. But surprisingly the quantisation of Hall resistance has only been observed once at zero magnetic field in exfoliated five-layer MnBi$_2$Te$_4$ flakes and is only limited to temperatures below 1.4 K, an order of magnitude lower than the Neel temperature[13]. Whilst exfoliated flakes have much better uniformity, the complexity of the fabrication process and device size on the scale of a few micrometres make epitaxial MnBi$_2$Te$_4$ thin films a more practical choice for mass production of macroscopic size devices. However, to date, electrical devices fabricated from MnBi$_2$Te$_4$ thin films perform worse than the exfoliated flake devices and the mechanism that leads to the suppressed quantisation in MnBi$_2$Te$_4$ thin films at zero magnetic field is yet to be understood. In particular, the quantisation of Hall resistance has yet to be observed at zero magnetic field and requires a magnetic field above the bulk spin-flop transition where the magnetic field forces the antiferromagnetic thin film into ferromagnetic order[14]. In addition to a magnetic field, the temperature must reach lower than 20 mK to achieve quantisation, which is a serious problem that must be addressed before considering the application of thin film devices[14].

MnBi$_2$Te$_4$ thin film samples have many advantages over an exfoliated flake sample as a platform for studying the mechanism of suppressed quantisation. The highly adjustable epitaxial growth process for the thin films enables one to vary sample stoichiometry, defect density, and to study the electronic properties of thin films grown under different conditions[15-18]. Moreover, the ultra-high vacuum (UHV) environment for the molecular beam epitaxy (MBE) film growth process and the macroscopic size of the sample allow spectroscopy and microscopy characterisation in UHV with minimal sample degradation. So far, there have been many studies on MnBi$_2$Te$_4$ bulk samples[19-21] where vast presence of magnetic defects has been reported. The magnetic defects are thought to cause sample inhomogeneity, but if and how the quantisation problem is linked to magnetic defects, and whether MBE thin film samples share the same problem as bulk samples remain elusive. On the other hand, research progress on MBE thin film samples falls behind, possibly due to the difficulty in sample growth and its air sensitive nature[22, 23]. The urgent demand for understanding the mechanism behind the stringent conditions required for achieving quantisation in thin film devices, therefore, motivates the investigation of the electronic properties and magnetic properties of MBE-grown MnBi$_2$Te$_4$ thin films.

In this review, we summarise recent advances in sample fabrication and electronic property characterisation of MBE-grown MnBi$_2$Te$_4$ thin films, aiming to present a clear picture from the perspective of experiments. This mini review consists of five sections. In the first section, we will introduce the material properties of MnBi$_2$Te$_4$ thin films such as thickness-dependent magnetic and electronic properties, and the thin film growth progress, followed by the second section: temperature-dependent studies on the topological phase transition of the electronic structure across magnetic transition temperature. In the third section we will present recent magneto-transport results on MBE grown MnBi$_2$Te$_4$ thin films. In the fourth section, we will discuss recent discovery on the mechanisms of suppression of QAHE due to magnetic disorder. In the last section, we will discuss heterostructure engineering as a promising strategy for realising QAHE at higher temperatures. The review ends with a conclusion and outlook for the QAHE.

The quantum anomalous Hall effect, an analogy of the quantum Hall effect without an external magnetic field, is characterized by quantized Hall resistance with vanishing longitudinal resistance at zero magnetic field. It features unique highly spin-polarised and dissipationless

chiral edge state conduction, which has great potential to lead the revolution of next-generation energy-efficient quantum devices.[10, 11] In 1988, Haldane proposed a simple tight-binding model in his seminal paper to demonstrate the possibility of quantized Hall resistance without an external magnetic field on a honeycomb lattice. Instead of an external magnetic field, a staggered potential with zero net magnetic flux is also able to produce quantized Hall resistance[24]. Although realization of such a lattice model in practice was not successfully achieved until 2014[25], Haldane's theory result offers invaluable insight to the QAHE: the role of external magnetic field can be replaced by time-reversal symmetry breaking, which then means QAHE can also be realised by introducing magnetic order. In addition to time-reversal symmetry breaking, non-trivial band topology was proven to be the second prerequisite soon after the advancement of topological band theory[8, 26]. However, in practice, finding material platforms satisfying both conditions is not a trivial task. First, the material must be a thin film with coupled top and bottom surface states due to the two-dimensional (2D) nature of QAHE. Second, QAHE requires the simultaneous presence of non-trivial band topology and broken time-reversal symmetry in the material. Lastly, the Fermi level of the material should be in the vicinity of the topological band gap such that the chemical potential can be effectively tuned into the gap using electrical gating. These prerequisites greatly narrow down the range of material candidates.

There have been several material systems where QAHE has been observed, including dilute magnetic doped topological insulator thin films[27-29] and moiré materials such as twisted bilayer graphene[30] and $MoTe_2$-WSe_2 heterobilayer[31]. Theoretically, the QAHE has been predicted in Kagome materials such as $Co_3Sn_2S_2$[32], Mn_3Sn[33], transition metal halide[34, 35] and metal-organic framework materials[36]. Recent calculations have also predicted the existence of QAHE in material systems without transition metal or magnetic elements such as silicene on SiC-(0001)[5], XY (X=K, Rb, Cs, Y=N, P, As, Sb, Bi) monolayers[6], and $VSiXN_4$ (X = C, Si, Ge, Sn, Pb) monolayers[7]. The orbital magnetism from partially filled p-states breaks time-reversal symmetry in these systems and the additional valley degree of freedom allows a combination of QAHE and valley effect. Among these candidate materials, $MnBi_2Te_4$, a magnetic topological insulator, has several advantages over conventional dilute magnetic doped topological insulators and other materials mentioned above for realising QAHE. In $MnBi_2Te_4$, the magnetic moments are incorporated into the crystal lattice rather than randomly distributed throughout the lattice as in the dilute magnetic doped topological insulators. Thus, there is less magnetic disorder and much better sample uniformity. Compared with twisted bilayer systems, the QAHE in $MnBi_2Te_4$ is not sensitive to twist angle, and thus is robust against local twist angle fluctuation due to strain relaxation. Furthermore, being a van der Waals material, exfoliation and growth of ultra-thin $MnBi_2Te_4$ has been done routinely[37-39], which is extremely difficult for Kagome materials because they are not van der Waals materials, and possess a 3D crystal structure and bonding. With these advantages and hosting both non-trivial band topology and robust net magnetisation, odd-layer $MnBi_2Te_4$ thin film is regarded as a promising system for realising QAHE beyond sub-Kelvin temperature.

The first realisation of QAHE was not reported until 2013 by Chang *et al.* in a dilute magnetic doped topological insulator thin film, where Cr, a magnetic dopant, is added to a topological insulator thin film to introduce long-range ferromagnetic order and break time-reversal symmetry, while preserving the non-trivial band topology of the film[3]. The ferromagnetic order opens up a magnetic gap in the Dirac cone and the Fermi level is adjusted close to the magnetic gap by adding Sb to Bi_2Te_3 as a substitutional dopant. While the hall resistance reached high quantisation of -0.987 $\frac{h}{e^2}$, the longitudinal resistance remains 0.098 $\frac{h}{e^2}$ at zero field, and its quantisation temperature is limited to no more than 30 mK[3]. The remnant longitudinal

resistance suggests the presence of dissipative pathways whose formation is attributed to the Dirac gap and doping fluctuations induced by a random distribution of the magnetic dopant throughout the thin film[40]. The magnetic gap fluctuation results in a significant reduction of the average band gap and the doping fluctuation brings the local Fermi level into the bulk states, forming puddles of metallic bulk states. In the end, the scattering from edge channels to conductive bulk states disfavours chiral edge state conduction[41]. For this reason, despite many techniques having been used, such as fine-tuning the doping concentration and co-doping, the quantisation temperature is limited to less than 300 mK in dilute magnetic doped topological insulator films[4]. One strategy for circumventing this problem is magnetic modulation doping where an interface layer with high concentrations of magnetic dopants is created to enhance the exchange coupling between the Dirac electron and magnetic order. The separation between the magnetic dopants and topological insulator layer reduces the effect from magnetic disorder, subsequently the quantisation temperature is improved to 1 K in a five-layer heterostructure structure, with longitudinal resistance of 0.081 $\frac{h}{e^2}$ [42]. However, even with the magnetic modulation doping method, the quantisation temperature is still an order of magnitude lower than the Curie temperature, which is attributed to Dirac mass gap fluctuations due to inhomogeneous distribution of magnetic dopant.

To solve the problem of magnetic disorder caused by dilute magnetic dopants, intrinsic magnetic topological insulator – $MnBi_2Te_4$ thin films have been proposed as a candidate material for high-temperature QAHE. In 2020, the QAHE was observed in an exfoliated five-layer $MnBi_2Te_4$ flake at 1.4 K without magnetic field, with Hall resistance quantized to 0.97 $\frac{h}{e^2}$ and longitudinal resistance below 0.061 $\frac{h}{e^2}$ [13]. Remarkably, the intrinsically ordered magnetic moment improves the quantisation temperature of QAHE, greater than the record achieved in magnetic modulation doped heterostructures and the best dilute systems[4, 29, 42]. However, the quantisation is still far from perfection: the activation gap of 0.64 meV extracted from temperature-dependent R_{xx} measurements is substantially lower than the theoretically predicted Dirac gap of 77 meV[43, 44], suggesting the presence of magnetic disorder. To understand the microscopic origin of the unexpected magnetic disorder and how it leads to the breakdown of QAHE, it is important to first discuss the layer-dependent magnetic and electronic material properties of $MnBi_2Te_4$ in the ultra-thin limit.

1. Material properties and film growth

$MnBi_2Te_4$ is a van der Waals material consisting of repeated stacking of individual septuple layers (SL) in the c-axis direction[43]. As shown in Figure 1(a), each septuple layer is made of seven atomic layers: Te-Bi-Te-Mn-Te-Bi-Te, with Mn^{2+} carrying magnetic moments and incorporated in the middle of each SL. $MnBi_2Te_4$ possesses intrinsic magnetic order in the crystal lattice. Within the same SL, the magnetic moments from the Mn^{2+} ions are aligned in the z-direction and are coupled through ferromagnetic (FM) interaction[43]. The intralayer 2D ferromagnetic order is stabilised by the magnetic anisotropy and the adjacent septuple layers are coupled by anti-ferromagnetic (AFM) interlayer interaction[44, 45] (Figure 1(a)). When the sample thickness is reduced to a-few SL limit, the effect of the uncompensated AFM SL on the surface becomes significant and the thin films show unique thickness-dependent electronic properties[43]. Figure 1(b) shows the band structure calculated using Density Functional Theory (DFT) with the insets indicating the magnetic order at different thicknesses. The value of the band gap and Chern number of $MnBi_2Te_4$ between 1-4 SL thickness are labelled. The combined effects of magnetic order and band topology result in unique thickness-dependent topological phases. At even layer thickness, the thin film is an axion insulator phase with AFM order, and at odd layer thickness, the thin film is a QAH insulator with uncompensated AFM order. The

band gap of the thin film decreases from 321 meV at 1SL to 97 meV at 4 SL as it gets thicker[43]. In a 5 SL film, the QAH insulator is predicted to have a band gap of 77 meV which is more than twice the value of typical dilute doped systems[40], holding the promise to overcome band gap fluctuation. Hosting different quantum phases at different thicknesses, $MnBi_2Te_4$ thin film becomes an ideal material platform for studying the axion insulator phase, QAH insulator phase, and their crossover at the interface of even and odd SL layers. Given the material properties are dictated by film thickness, MBE becomes the best method for fabricating $MnBi_2Te_4$ thin films with controlled thickness, for its capability of achieving high-quality layer-by-layer epitaxial film growth with clean interface.

The growth of high-quality epitaxial $MnBi_2Te_4$ thin films have been reported on many substrates including Si (111)[46, 47], sapphire (0001)[22, 48, 49], Graphene/SiC (0001)[50, 51] and $SrTiO_3$ (111)[52, 53]. Among these substrates, the growth on Si (111) requires using Te as a wetting layer on the immediate substrate surface to improve subsequent septuple layer growth[12] and the growth on sapphire substrates requires pre-growth annealing treatment to create oxygen vacancies or deposition of Bi_2Te_3 as a wetting layer which also needs to be annealed to create a uniform surface layer[48]. Compared to Mn-doped Bi_2Te_3, the growth of $MnBi_2Te_4$ needs much higher Mn flux and the incorporation of the magnetic Mn layer is crucial. Generally, there are two ways of growing $MnBi_2Te_4$ thin films via MBE (Figure 1(c)). The first growth method is the co-deposition of Mn, Bi and Te simultaneously, which requires fine-tuning the flux ratio of the elements to avoid the formation of additional MnTe or Bi_2Te_3 phases[48, 51]. The second growth method, the layer alternating method, as depicted in Figure 1(c) (ii) is a more reliable growth method where a bilayer of MnTe is grown on top of a quintuple layer Bi_2Te_3 followed by an annealing process to facilitate the spontaneous rearrangement of the MnTe and Bi_2Te_3 layers into one SL of $MnBi_2Te_4$ [12, 53]. Luo *et al.* recently reported a systematic study of MBE growth of $MnBi_2Te_4$ thin films under different growth conditions such as substrate temperature, Mn/Bi flux ratio and Bi flux rate. The $MnBi_2Te_4$ phase exists in a narrow temperature window in the thermodynamic phase diagram. Ideally, if one adjusts substrate temperature and element composition carefully, instead of forming separated MnTe and Bi_2Te_3 phases, bilayer MnTe tends to intercalate into quintuple layer Bi_2Te_3, forming the $MnBi_2Te_4$ SL structure. In practice, Luo *et al.* found Bi_2Te_3 and MnTe impurity phases can only be minimised by optimising the flux ratio and the complete elimination of the impurity phase is very difficult. Additionally, the impurity phases cannot be eliminated by performing post-annealing either[48]. Nevertheless, layer-by-layer growth of high-quality $MnBi_2Te_4$ thin films with stoichiometry close to 1:2:4 has been routinely demonstrated[46, 51-53]. The accurate thickness control down to just a single layer and large sample area makes MBE-grown $MnBi_2Te_4$ films an excellent choice for studying the thickness-dependent properties.
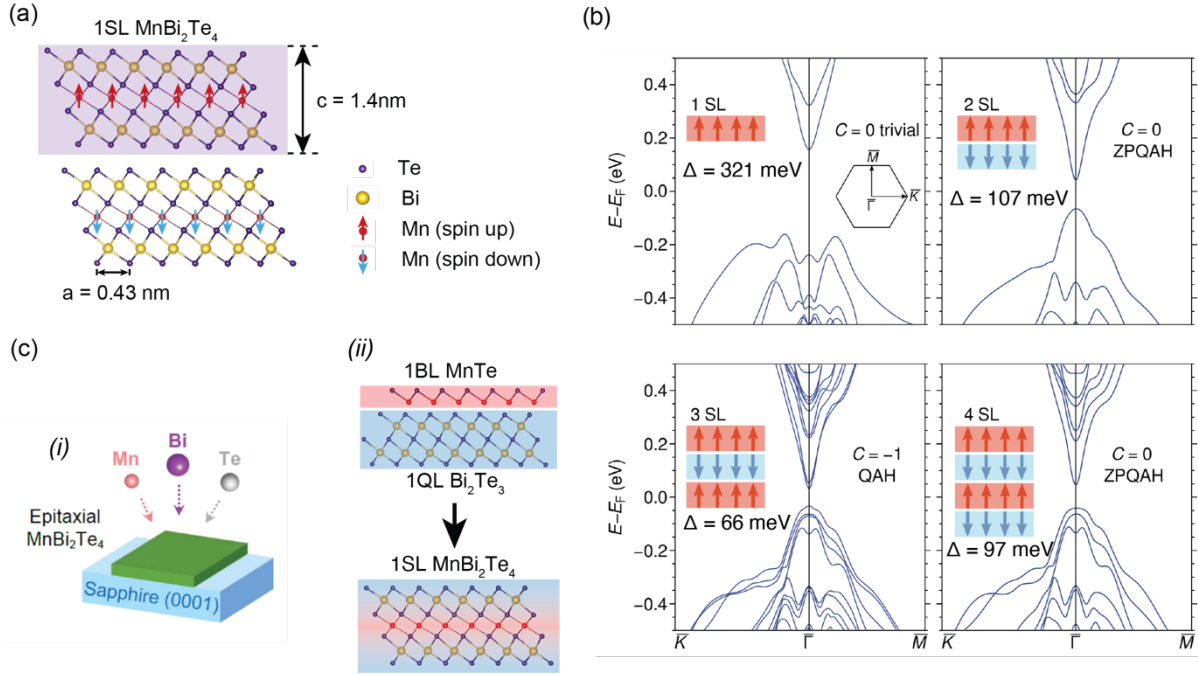
Figure 1 Basic properties of MnBi$_2$Te$_4$ thin films and their epitaxial growth method. (a) Crystal structure of a 2 SL MnBi$_2$Te$_4$ thin film where lattice constants are labelled. The shaded area represents the definition of a septuple layer, and the red arrows represent the magnetic moments on Mn^{2+} ions. (b) Thickness-dependent band structure calculated from Density Functional Theory (DFT) labelled with band gaps and Chern numbers that indicate the topological phase of the thin film at different thickness. (c) Illustration of the two growth methods reported for MnBi$_2$Te$_4$ thin film: (i) co-evaporation of three elements and (ii) layer alternating method. Reproduced from ref. [14] with permission from Oxford Academics, copyright 2024 and ref. [54] with permission from American Physical Society, copyright 2019.

Figure 2(a) is a typical scanning tunnelling microscopy (STM) scan showing the surface topography of a MnBi$_2$Te$_4$ thin film grown on Si (111), where in the scan region the majority of the thin film has the thickness of 4 SL with 5 SL islands on top[54]. The topography image indicates that in the MBE MnBi$_2$Te$_4$ thin film, it is common to have a non-uniform thickness of SL terraces, which is typically on a scale of a few hundred nanometres. The septuple layer terraces are often accompanied by dispersed bilayer MnTe or quintuple layer Bi$_2$Te$_3$ domains. Figure 2(b) and 2(c) are the magnetic circular dichroism measurements of MnBi$_2$Te$_4$ thin films of different thicknesses where the magnetic transition temperature can be extracted from the onset of the reflective magnetic circular dichroism curve[39]. The magnetic transition temperature of the thin films increases with the film thickness from 15 K in 1 SL to eventually saturating at 25 K for 10 SL thickness, which corresponds to the Neel temperature of bulk MnBi$_2$Te$_4$. In Figure 2(d), angle-resolved photoemission spectroscopy (ARPES) spectra of MnBi$_2$Te$_4$ thin films between 1, 2, 3, and 5 SL demonstrate the thickness-dependent electronic structure[46]. At 1 SL thickness, the substantial quantum confinement effect contributes to a large indirect band gap of about 350 meV and the thin film is in a trivial ferromagnetic insulator phase. When the thickness increases to 2 SL, the quantum confinement effect becomes weaker and more importantly, the additional composite parity-time reversal (*PT*) symmetry from crystal inversion and time reversal operation results in double degenerate bands and a Chern number of zero[43, 55]. If the AFM order is aligned by the external magnetic field into FM order, the Chern number becomes ±1 depending on the magnetisation direction and a chiral edge state appears on the sample edge. The thin film is, therefore, in an axion insulator phase or a zero-plateau quantum anomalous Hall phase[43]. At 3 SL thickness, the additional uncompensated septuple layer on the surface contributes net magnetisation. Combined with the non-trivial band

topology, a Dirac cone shows up in the electronic structure of 3 SL film and the film enters a QAH phase. Similarly, 5 SL film also hosts a QAH phase. As the film thickness further increases, the quantum confinement becomes much less significant and the $MnBi_2Te_4$ oscillates between QAH insulator (odd SL) and axion insulator (even SL) phases until it reaches an AFM TI phase in the bulk form[56].
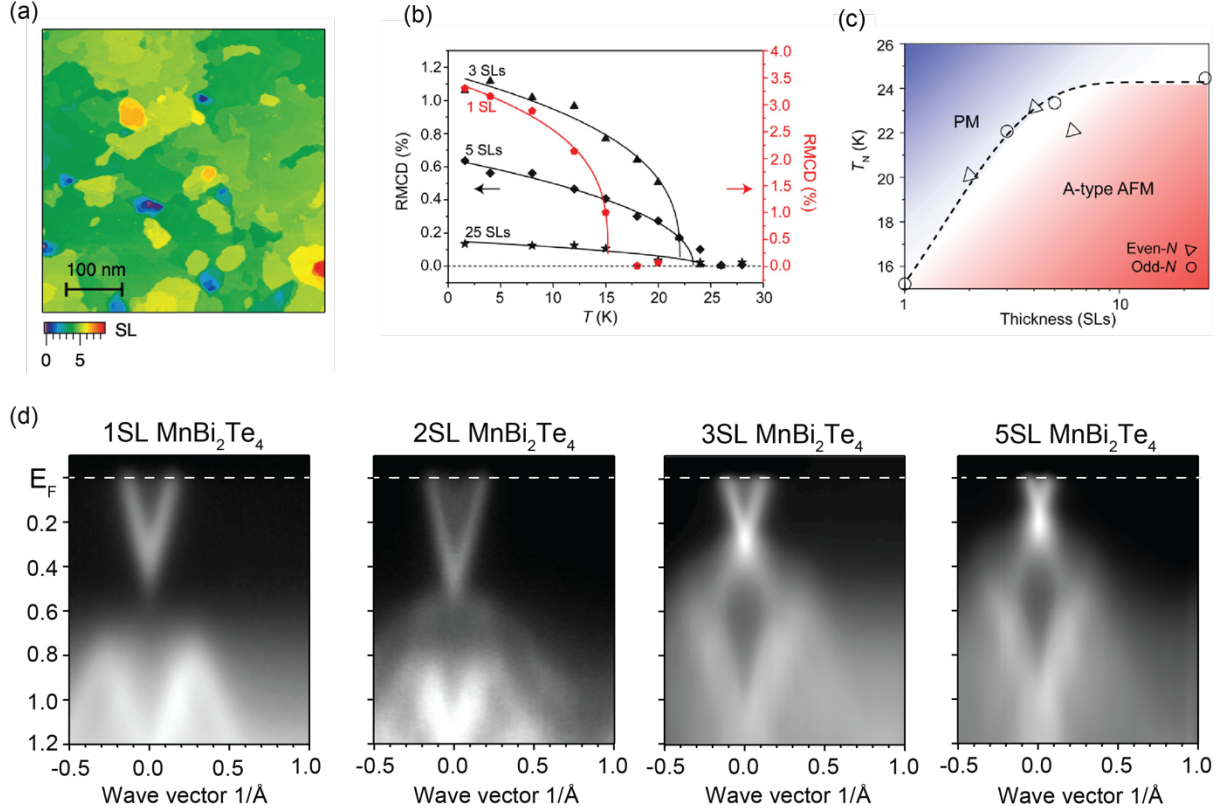
**Figure 2 Thickness-dependent properties of MnBi₂Te₄ films.** a) Large-area scanning tunnelling microscopy topography image showing the topography of the surface of a 5SL film (-2V, 20 pA). b) Temperature-dependent reflective magnetic circular dichroism measurements for MnBi₂Te₄ films of different thickness. c) Magnetic phase diagram and magnetic transition temperature extracted from b). d) Thickness-dependent angle-resolved photoemission spectroscopy (ARPES) spectra of MnBi₂Te₄ films along GM direction. Reproduced from ref. [39] with permission from American Physical Society, copyright 2021, ref. [46] with permission from American Chemical Society, copyright 2021, and ref. [55] with permission from Wiley, copyright 2024.

2. Topological phase transition across Neel temperature

To understand the lack of QAHE in MBE-grown $MnBi_2Te_4$ thin films and what causes the temperature-induced breakdown of QAHE below Neel temperature, we need to examine the evolution of the electronic structure across the magnetic transition temperature in $MnBi_2Te_4$ thin films. Figure 3 shows a summary of temperature-dependent ARPES and scanning tunnelling spectra of thin films at different thicknesses from recent reports. In Figure 3(a)-(b), Xu *et al.* measured 2 SL, 3 SL and 6 SL thin films across their Neel temperatures. Only 3 SL sample shows clear change of band structure approximately between 7-18 K. Although it is difficult to resolve in the energy dispersion spectrum, the energy distribution curves (EDC) extracted at normal emission show a slight decrease of spectral weight in the bands near the gap whereas the even layer samples show indistinguishable change. Further investigation at different photon energies and temperatures is required to understand the temperature-dependent electronic band structure in even-layer $MnBi_2Te_4$ thin films. In the case of 5 SL $MnBi_2Te_4$, the thickness where QAHE is observed in the transport experiment on exfoliated

flakes, Figure 3(c) is a schematic demonstrating the magnetic ordering and expected band structure below and above Neel temperature[46]. It is expected that as the temperature is raised above Neel temperature, the thin film becomes paramagnetic and the magnetic gap in the Dirac surface state closes. The restoration of time reversal symmetry means the thin film is no longer in the QAH phase, thus, the chiral edge state is absent. Indeed, this gap-closing transition has been observed in previous temperature-dependent ARPES experiments[46], as shown in Figure 3(d)-(e). The temperature-dependent ARPES spectra are taken from 8 K to 33 K. EDCs extracted from normal emission at 8 K and 13 K are plotted in Figure 3(d) to compare the Dirac gap at Gamma point. The width of the EDC peak decreases as the sample is warmed up to 13 K, the signature of a gap-closing phase transition. Following a similar analysis, the Dirac gap as a function of temperature is plotted in Figure 3(e) and the trend indicates the Neel temperature for the 5 SL MnBi$_2$Te$_4$ MBE thin film is somehow between 8 to 13 K, which is almost half of the value in Figure 1(b). The low Neel temperature observed may indicate that the magnetic order depends on the MBE film sample quality. Additionally, the ARPES spectra of 5 SL MnBi$_2$Te$_4$ film show a very strong spectral signal in the Dirac gap. Although the matrix element effect from Te p_z states has been proposed as an explanation[57], another possibility is the spectral weight arises from gapless or reduced gap regions, and these fluctuations may appear as additional spectral weight in the band gap which will be discussed later in section 4. Lastly, the vanishing Dirac gap has also been reported in scanning tunnelling spectroscopy (STS) measurements at 77 K on a 5 SL film grown on Graphene/SiC in Figure 3(f)[51], which further supports the ARPES results.
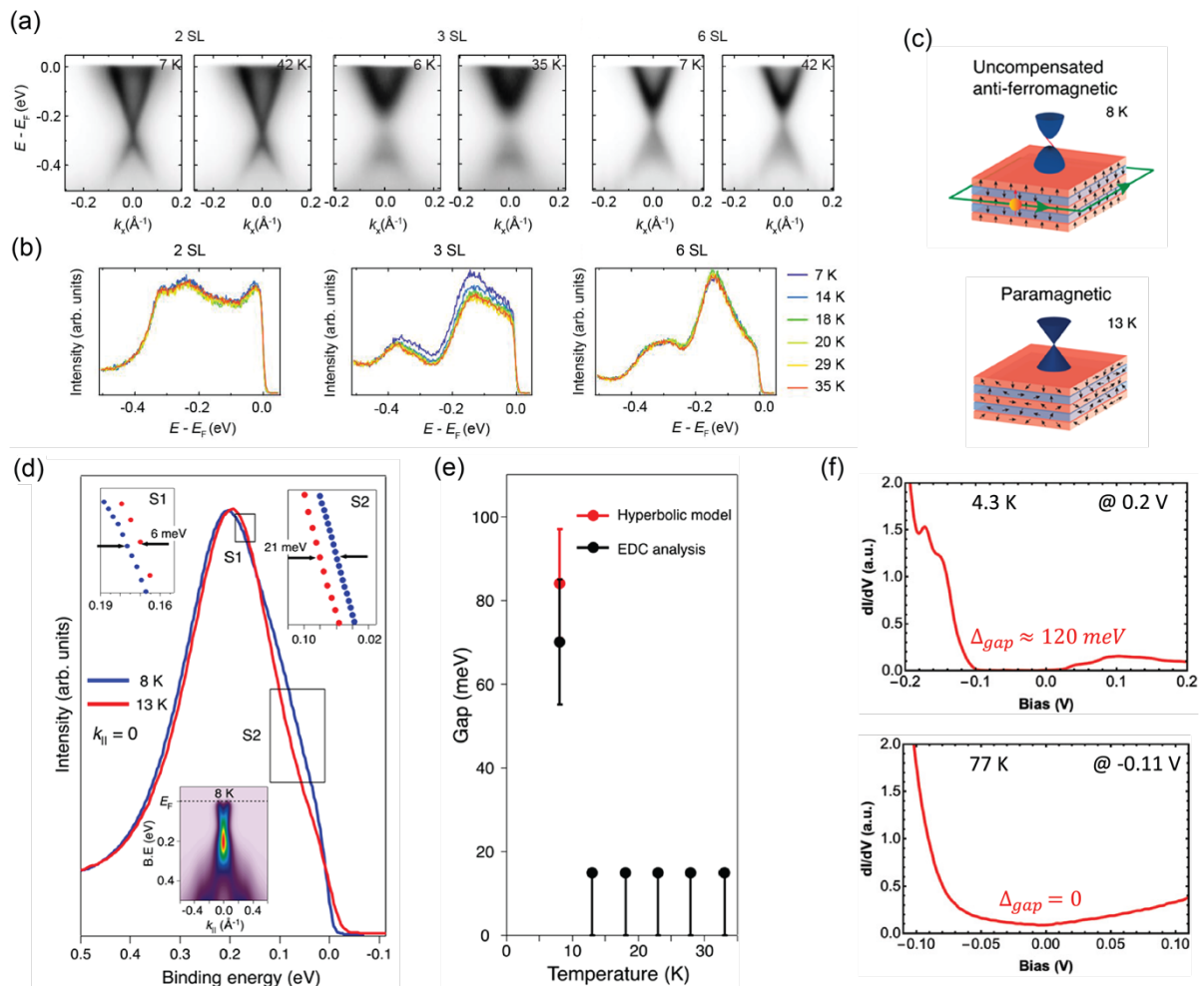
Figure 3 Summary of temperature-dependent measurements on MnBi$_2$Te$_4$ MBE thin films. a) ARPES spectra of 2 SL, 3 SL, and 6 SL MnBi$_2$Te$_4$ measured with a 7 eV laser source. b) Energy distribution curves (EDC)

taken at normal emission at different temperatures across magnetic transition temperature. c) Schematics showing the magnetic order and corresponding surface states and edge states below and above the Neel temperature. d) EDCs taken at normal emission from a 5 SL MnBi$_2$Te$_4$ thin film at 8 K and 13 K, insert: ARPES spectrum of the 5 SL thin film where EDCs are taken. e) Dirac gap as a function of temperature across Neel temperature in a 5 SL thin film. f) Scanning tunnelling spectra taken at 4.3 K and 77 K on a 5 SL thin film. Reproduced from ref. [46, 52] with permission from American Chemical Society, copyright 2021, and ref. [51] with permission from National Academy of Science, copyright 2022.

3. Electronic transport on MnBi$_2$Te$_4$ thin films

Unlike exfoliated MnBi$_2$Te$_4$ flakes where quantisation of Hall resistance has been observed at zero magnetic field, achieving quantisation of the Hall resistance and near zero longitudinal resistance in MBE thin film samples appears to be much more challenging. As reported by Bai *et al.*[58] and shown in Figure 4(b)-(c), 5 SL MnBi$_2$Te$_4$ grown via MBE at zero magnetic field possesses a Hall resistance of only 0.34 $\frac{h}{e^2}$, whilst the R_{xx} is significantly larger than the 0.061 $\frac{h}{e^2}$ reported in 5 SL exfoliated flakes. In order to achieve quantisation, a magnetic field of 9 T is required to reach $R_{xy} = 0.98 \frac{h}{e^2}$ and $R_{xx} = 0.20 \frac{h}{e^2}$ at 20 mK where the AFM order is forced into FM order by the external magnetic field that exceeds spin-flop fields. In other words, quantisation is only achieved in the FM configuration. The temperature dependence of R_{xx} at high field indicates the QAH state as the ground state of the film but the high R_{xx} and low R_{xy} in the low field regime suggests a rather insulating state that lacks continuous chiral edge channels over the length scale of sample size[14]. The large R_{xx} observed may come from nonuniform terrace thickness and tunnelling process between disconnected QAH domains. The authors have also discovered prolonged annealing treatment on the film improves robustness of R_{xy} quantisation but deteriorates R_{xx} substantially. Their results provide transport evidence of suppressed QAHE and suggest that sample inhomogeneity makes realising QAHE much more challenging in MBE-grown MnBi$_2$Te$_4$ thin films. In the formation process of septuple layers, the diffusion process of Mn through the film and energy favourable anti-sites formation inevitably introduces high density of defects, and impurity phases such as Bi$_2$Te$_3$. Furthermore, the single crystal grain size is often much smaller than flakes obtained from exfoliating bulk crystals. A recent study on thickness-dependent anomalous Hall measurements by Zhao *et al.* reveals the evolution of two anomalous Hall components in MnBi$_2$Te$_4$ thin films from 2 SL to 7 SL[53]. They discovered the sign of the first component shows striking layer dependence and the hysteresis diminishes as the film gets thicker whereas the second component shows monotonic decrease as the film thickness increases. The coexistence of both components indicates a contribution from both layer dependent AFM order and from an impurity phase of Mn doped Bi$_2$Te$_3$ based on the different magnetic transition temperatures for the two components. Interestingly, the hysteresis in the Hall resistance was observed in all even layer samples and is strongest in a 2 SL thin film and weakest in the 6 SL thin film. Ideally, even layer films in the collinear AFM phase are not expected to show anomalous Hall effect and the observed anomalous Hall effect in even layer thin films indicates remanent net magnetisation. One may propose an explanation that the non-uniform thickness of the MBE thin films can lead to the hysteresis in even layer thickness, however, several previous magnetometry studies on exfoliated flakes of even layer thickness also show a net magnetisation[39, 59]. The definitive layer thickness in the exfoliated sample precludes this possibility. Therefore, the anomalous Hall effect in the even layer MnBi$_2$Te$_4$ thin films is more likely to originate from substrate induced effect or magnetic disorder. The diminishing net magnetisation in thicker even layer films favours contribution from the substrate effect where additional magnetisation can be induced by an interface dipole field arising from charge transfer. Furthermore, the coercive

field reported for even layer films is typically between 1 to 2 T, which is bigger than the field strength for overcoming magnetic disorder[54]. Magnetic disorder tends to induce local spin fluctuations, which should be more likely to reduce the magnetisation instead of increasing net magnetisation. The magneto-transport results discussed above reflect the global transport properties of the $MnBi_2Te_4$ thin films and provide critical information on the magnetic and transport properties of the chiral edge channels on a macroscopic scale. In 2D topological insulators such as WTe_2, scanning probe techniques such as microwave impedance microscopy (MIM)[60] and scanning tunnelling microscopy and spectroscopy (STM/STS)[61] are used to probe the edge state. MIM is capable of mapping conductance spatially on a length scale over micrometres and STM/STS offers information from local density of states with superb energy resolution only depending on the temperature with sub-nanometre spatial resolution. To understand the microscopic mechanism that prevents quantisation, we need to examine the electronic properties on the nanometre scale and STM/STS is the primary choice.
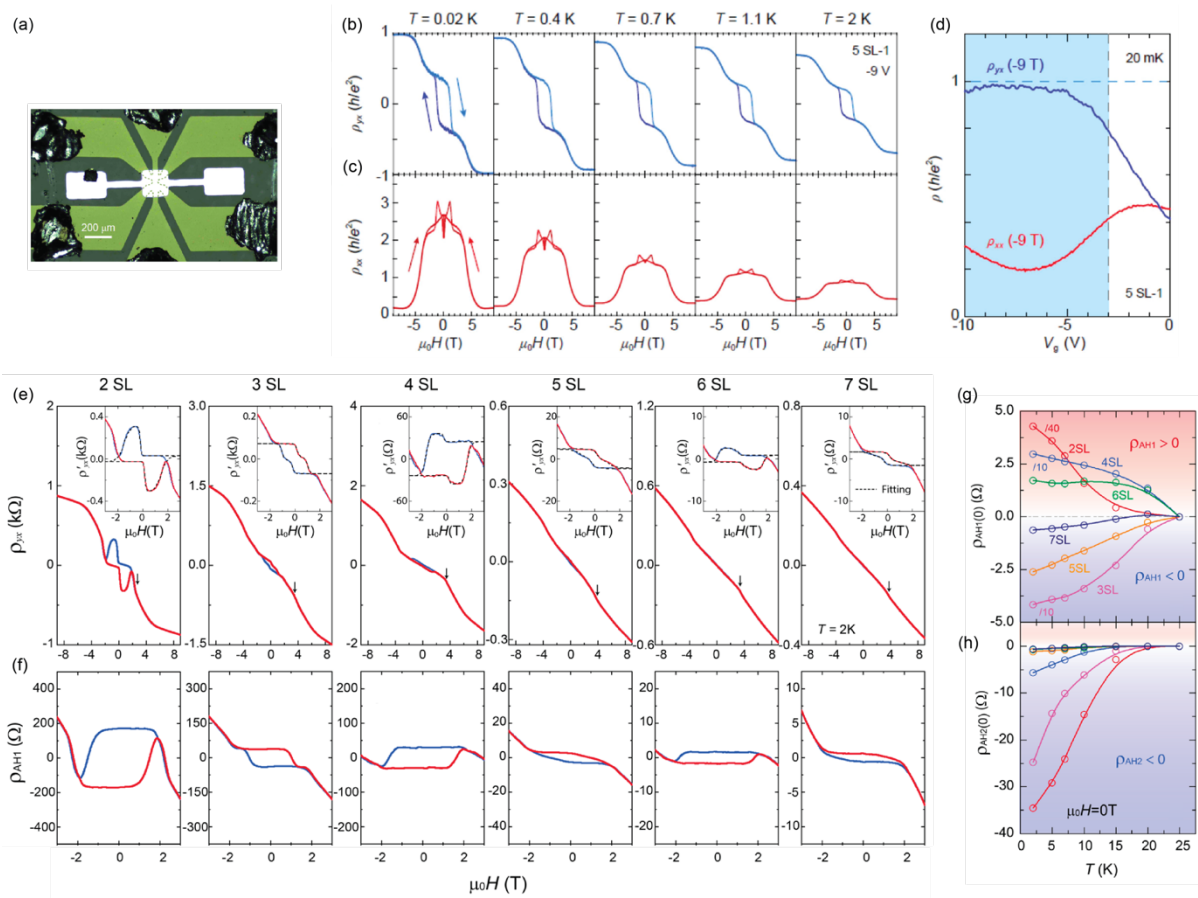
Figure 4 Transport results on 5 SL $MnBi_2Te_4$ MBE thin films and thickness-dependent anomalous Hall effect measurements. a) Optical image of a 5 SL Hall bar device. b-c) temperature-dependent magneto-transport measurements with chemical potential tuned in the band gap. d) Gate dependent longitudinal (red curve) and Hall resistivity (blue curve) in a 9 T magnetic field at 20 mK. e) Thickness-dependent Hall resistivity as a function of magnetic field and f) anomalous Hall resistance component extracted from e). The blue/red represents decreasing/increasing magnetic field. g)-h) temperature dependence of two anomalous Hall components extracted for different film thickness. Reproduced from ref.[53] with permission from American Chemical Society, copyright 2021 , and ref. [14] with permission from Oxford Academics, copyright 2024.

## 4. Reveal the mechanism of QAHE suppression - Limitation

Currently, the biggest limitation of the QAHE in $MnBi_2Te_4$ is the low quantization temperature and requirement of magnetic field to reach quantization at higher temperature. The mechanism

of the QAHE suppression has been under active investigation. A promising explanation is that the magnetic disorder on the surface induces Dirac gap fluctuation, leading to puddles of metallic bulk state and coupling to the edge state[54]. To date, the majority of STM studies focus on cleaved surface of bulk crystals. In cleaved bulk crystals, large amounts of anti-site defects including Bi_{Te}, Mn_{Bi}, and Bi_{Mn} have been discovered[21] and the tunnelling spectra show negligible response to external magnetic field even above spin flop field[19]. Moreover, none of the bulk studies observed a Dirac gap on the surface and the evidence of surface gap induced by exchange coupling is still lacking. The discovery in bulk crystals raises several questions for thin film samples: does the thin film also have a large amount of anti-site defects, does the electronic structure of thin film show response to magnetic field, and most importantly, is there a chiral edge state on the sample edge of a 5 SL thin film $MnBi_2Te_4$? In practice, performing STM measurements on the sample edge of a 5 SL thick film is very challenging given the MBE film grows in the layer-by-layer mode. Fortunately, because $MnBi_2Te_4$ thin film shows layer-dependent Chern number[43], instead of probing edge state on the 5 SL sample edge, one can look for edge states on the step edge between a 5 SL and a 4 SL terrace.

Recently, Li *et al.* reported the presence of magnetic disorder in a 5 SL $MnBi_2Te_4$ thin film and observation of the edge state on the 5 SL to 4 SL step edge[54]. Ideally, in a quantum anomalous Hall phase, the Dirac band in the bulk of the material should be all gapped by the exchange interaction from the magnetic order and only the edge of the sample remains gapless due to the presence of chiral edge state. This scenario is depicted in the green band schematics in Figure 5(a). Figure 5(b) demonstrates the spatial distribution of electron density of states measured within the Dirac band gap in the same region as Figure 5(a) where continuous 1D spectral intensity is clearly visible parallel to the step edge. Surprisingly the density of states (DOS) in the interior of the sample away from the edge remains large in certain areas (white bright puddles in Figure 5(b). These bright puddles with high local DOS show metallic behaviour, i.e. metallic puddles from local tunnelling spectroscopy measurements. In Figure 5(c), STS taken from the edge state (red), metallic puddles (black) and insulating bulk regions (purple) represent the three different types of regions in the DOS map (Figure 5(b)) based on their spectral features. Although the STS curves from insulating bulk regions possess a Dirac gap, the STS curves taken from the metallic puddles resemble gapless Dirac states. They have much stronger dI/dV signal than the edge state and the insulating bulk state. In addition, most importantly, the metallic puddles connect to the edge state in some areas, potentially acting as dissipative current channels that drain the edge state current and contribute to remnant ρ_{xx} component in the transport measurements.

To understand the formation of the metallic puddles, the Li et al., mapped the distribution of Dirac band gap on the same 5 SL terrace and discovered significant spatial fluctuation of Dirac band gap on the length scale much larger than the size of point defects. The Dirac band gap fluctuation on a 5 SL terrace is further supported by Liu *et al*[51]. In the STS taken at 6 different locations in Figure 5(d)-(e) by Liu et al., the band gap is only discernible at location 1 and 2 and the other locations remain gapless, suggesting Dirac gap fluctuation over the length scale of several nanometres. Li *et al.* then performed the Dirac band gap map over a large area and studied how the gapless regions respond to a magnetic field of 1 T (Figure 5(f)-(h)). They found a 1 T magnetic field is enough to restore the majority of the Dirac gap on the 5 SL terrace. The Dirac band gap in the gapless regions at 0 T can be restored to almost 45 meV by applying a 1 T external magnetic field which is well below the surface spin flop field of 2 T[62]. This discovery indicates that the increase of Dirac band gap is not related to the spin flop transition. Instead, the 1 T field strength required to restore the Dirac band gap is evidence of magnetic disorder on the 5 SL terrace. One possible origin of the Dirac gap fluctuation proposed by Li

et al. is the magnetic disorder in the Mn^{2+} ions layer located in the middle of the uncompensated SL on the surface, but verifying this hypothesis requires future investigation using techniques such as spin-polarised STM and high-resolution magnetic force microscopy measurements. There have been several recent studies suggesting complex competing magnetic interactions in $MnBi_2Te_4$[63] and the possibility of magnetic disorder induced by the large number of anti-sites *via* strong *p-d* hybridisation[64]. However, what exactly causes the magnetic disorder still remains an open question. Nevertheless, the observed coupling between edge state and metallic puddles in Figure 5(b) and prevalent Dirac band gap fluctuation suggest magnetic disorder is a universal problem not only in MBE thin film but also in exfoliated flakes given their similarity. Magnetic disorder is the most microscopic level mechanism that leads to the breakdown of QAHE, and it must be overcome in $MnBi_2Te_4$ in order to achieve better quantisation in MBE thin films. By reducing magnetic disorder, essentially the dissipative bulk conduction channels and their coupling to edge state channels are reduced as well at the same time, leading to a lower longitudinal resistance, a higher degree of quantisation of Hall resistance and a larger average Dirac band gap that is essential for overcoming thermal fluctuation. On top of the magnetic disorder, the next possible breakdown mechanism for QAHE on a larger length scale proposed by Bai *et al.* is the chiral edge state tunnelling across grain boundary between $MnBi_2Te_4$ domains, which requires optimising growth condition to obtain domains at least of several micrometres[14]. It is also important to minimise variation in the layer number on the length scale of micrometres so that the axion insulator phase at even layer thickness does not contribute additional $\rho_{xx} \sim \frac{h}{e^2}$ to the QAHE[14]. Last but not least, the Mn-doped Bi_2Te_3 impurity phase must be eliminated. The difference in doping level, additional magnetic interaction and scattering at the phase boundary between $MnBi_2Te_4$ and the impurity Bi_2Te_3 phase can further prevent quantisation of the Hall resistance. In the last section, we will discuss several strategies for overcoming the magnetic disorder problem and realising QAHE in $MnBi_2Te_4$ MBE films.
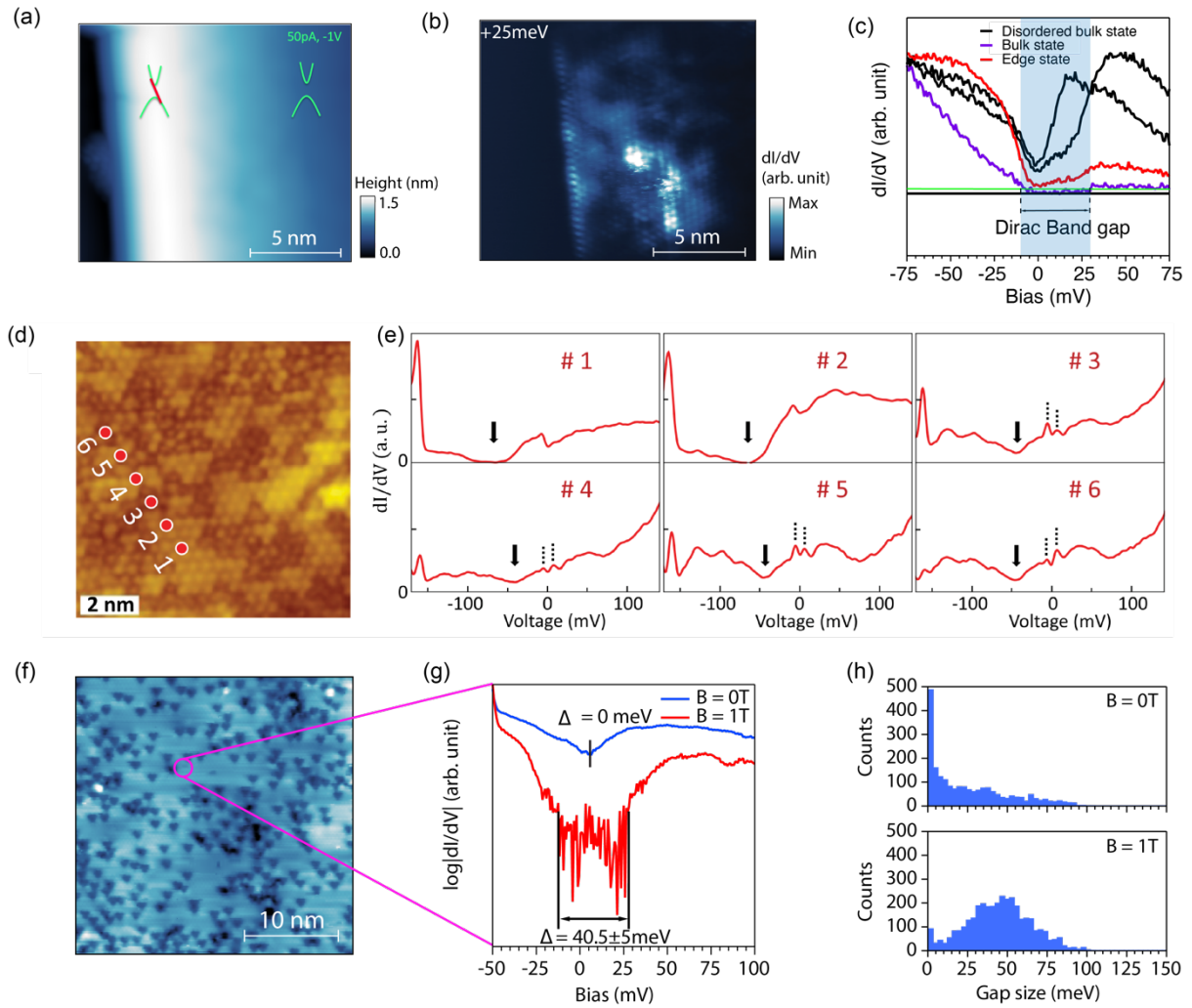
Figure 5 Scanning tunnelling microscopy and spectroscopy studies on 5 SL MnBi₂Te₄ thin films. a) Topography of a 4 SL to 5 SL step edge (50 pA, -1 V). The spatial distribution of the Dirac gap is illustrated by the green sketches. b) Density of state map in same region as a) taken at +25 meV bias showing spatial distribution of edge state and metallic puddles from disordered bulk states. c) Scanning tunnelling spectra (STS) measured for edge state, bulk state, and disordered bulk states. d) Topography of a 5 SL terrace in a different work by Liu et al. e) STS taken from locations in d) with gapped region marked. f) Topography of a 5 SL terrace where large amount of point defects are visible. g) STS curves taken from the purple circle in f) at 0 T and 1 T applied perpendicular magnetic field with Dirac gap labelled. h) histograms of Dirac gaps extracted from region in f) at 0 T and 1 T. Reproduced from ref.[55] with permission from Wiley, copyright 2024, and ref. [51] with permission from National Academy of Science, copyright 2022.
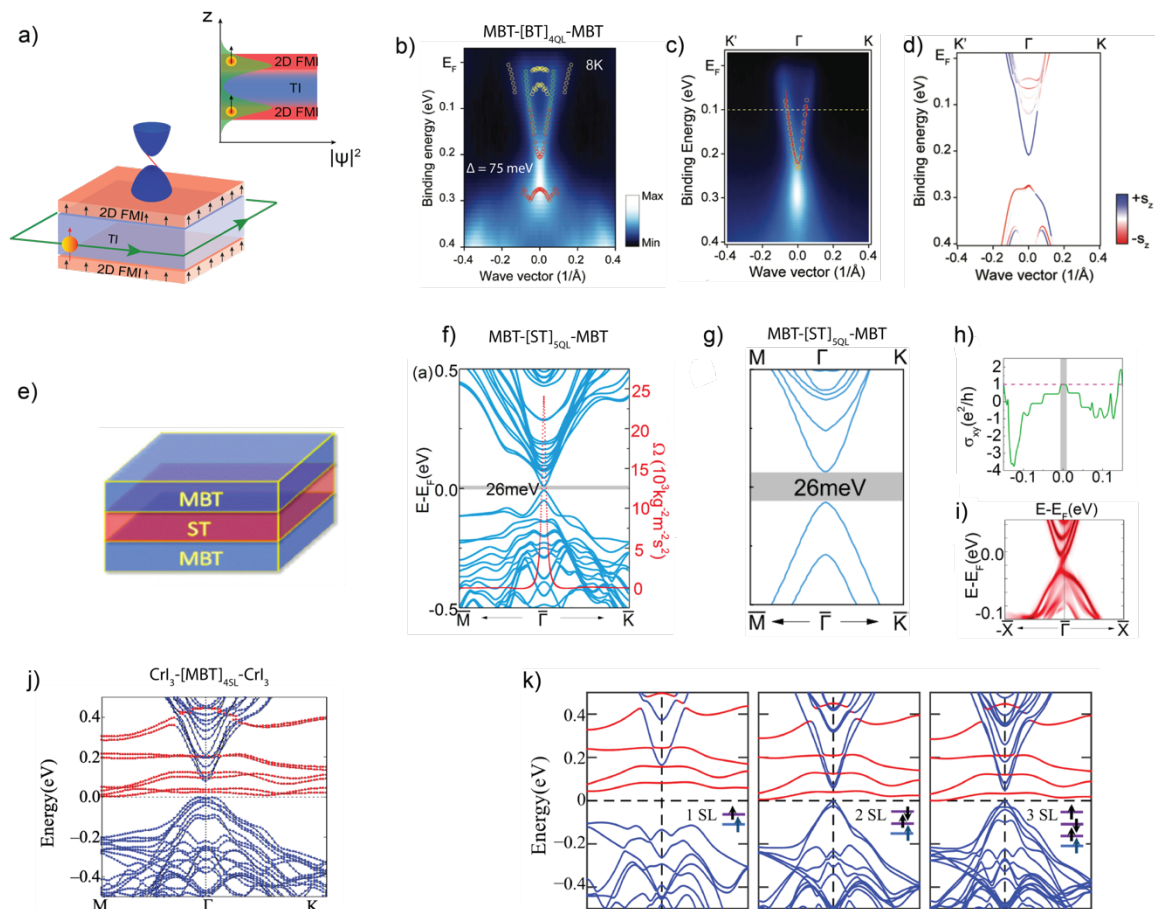
5.   Realising QAHE at a higher temperature - Heterostructure engineering

The QAHE realised in 5 SL MnBi₂Te₄ demonstrated that intrinsic magnetic order indeed improves the quantisation temperature from sub-millikelvin to 1.4 K at zero magnetic field. However, as we discussed above, problems including edge state-bulk state coupling, sample non-uniformity and magnetic disorder need to be resolved to further improve the quantisation temperature. We are still far from realising QAHE at room temperature or even at 77K because the highest possible QAHE quantisation temperature is set by the magnetic transition temperature of the material. In the case of 5 SL MnBi₂Te₄, the maximum temperature one can observe the QAHE is 25 K, which is the Neel temperature of the material. Going beyond 25 K requires the discovery of new materials with higher magnetic transition temperatures, that still possess large magnetic gaps. One particularly promising strategy is heterostructure engineering

which essentially separates the magnetic order from the chiral edge channel. Mogi *et al.* engineered sandwich heterostructures consisting of ferromagnetic layers Cr doped $(Bi, Sb)_2Te_3$ and topological insulator layers $(Bi, Sb)_2Te_3$ and achieved high quantisation temperature of 1 K[42]. The separation of topological insulator layer from the ferromagnetic layer reduces Dirac band gap fluctuation and allows one to use a higher concentration of magnetic dopants. However, the materials for ferromagnetic layer and topological insulator layer must be carefully chosen because a large lattice mismatch would not improve the quantisation temperature even if the ferromagnetic layer has strong magnetic order[65, 66]. It is desirable that the two layers have minimal lattice mismatch to reduce the interface potential and achieve maximal exchange interaction between topological states and magnetic moments. The discovery of $MnBi_2Te_4$ and other 2D ferromagnets expands the material category for engineering ferromagnet- topological insulator – ferromagnet heterostructures, see Figure 6(a) for a schematic of the heterostructure. Specifically, 1 SL $MnBi_2Te_4$, a ferromagnetic insulator with a band gap of more than 300 meV and Cuire temperature of 15 K, can be used to induce a sizable magnetic band gap in the top and bottom surface state of a topological insulator such as Bi_2Te_3, Sb_2Te_3 or their alloy compound[67]. The heterostructures host a QAH phase independent of the topological insulator layer thickness. Compared with the dilute magnetic doped ferromagnet layer used in ref.[42], the intrinsic magnetic order in $MnBi_2Te_4$ is more robust and its heterostructure formed with Bi_2Te_3, Sb_2Te_3 can potentially increase quantisation temperature. In a recent ARPES study on the $MnBi_2Te_4$ –$[Bi_2Te_3]_{4QL}$- $MnBi_2Te_4$ heterostructure, a 2D Dirac gap of 75 meV, or equivalent to three times the thermal energy at room temperature (25.9 meV), has been observed at 8 K, as shown in Figure 6(b)[68]. The observed large Dirac gap implies the heterostructure is more robust against Dirac band gap and doping fluctuation. To confirm the magnetic nature of the gap, the authors measured energy dispersion along ΓK direction where a combined effect of strong hexagonal warping ($418\ eV \cdot Å^3$) and exchange coupling (75 meV) produces asymmetry in band dispersion about Γ point, evidence of broken time reversal symmetry. In addition, the Dirac electron band along ΓK direction is spin-polarised below 0.12 eV, according to the DFT calculation (Figure 6(d)). The large magnetic gap reported in the heterostructure formed by $MnBi_2Te_4$ and Bi_2Te_3 confirms the enhanced exchange coupling due to the magnetic extension effect. However, the Fermi level from ARPES spectra sits in the bulk conduction band, quite far from the gap region which is required to observe QAHE in a transport measurement [68]. One possible strategy would be to use Sb_2Te_3 to alloy with the Bi_2Te_3 layer and *p*-dope the heterostructure so that the gap region can be accessed by electrostatic gating. Another possibility based on a recent theory prediction is to replace the Bi_2Te_3 layer with an Sb_2Te_3 to yield a $MnBi_2Te_4$ –$[Sb_2Te_3]_{5QL}$- $MnBi_2Te_4$ heterostructure, as shown in Figure 6(e)[69]. The introduction of Sb_2Te_3 raises the Curie temperature up to 42 K which is almost twice as much as the Curie temperature in the Bi_2Te_3 based heterostructure[69]. Although the heterostructure has a smaller Dirac gap of 26 meV (Figure 6(f)-(g)), the gap size is still comparable to room temperature thermal energy (25.9 meV). The heterostructure is theoretically predicted to host a quantum anomalous Hall phase by calculation of quantised Hall conductance (Figure 6(h)) and chiral edge state dispersion (Figure 6(i)). Therefore, adding Sb_2Te_3 to the Bi_2Te_3 layer not only potentially tunes the Fermi level, but also increases the magnetic transition temperature. The size of the magnetic gap and improved magnetic transition temperature in a $MnBi_2Te_4$ –$[(Bi, Sb)_2Te_3]_{nQL}$- $MnBi_2Te_4$ heterostructure make it a promising candidate material for realising QAHE well above 2 K. Alternatively, another strategy is to use another 2D ferromagnet such as CrI_3 or $CrBr_3$ to proximitise the $MnBi_2Te_4$ film. A monolayer ferromagnet layer can be assembled using heterostructure stacking techniques[70], or it can be grown by depositing CrI_3 precursor molecules on the substrate or $MnBi_2Te_4$ films[71]. These ferromagnet have a much higher Curie temperature of 45 K[72] and can align the magnetic moments in the $MnBi_2Te_4$ with additional

exchange coupling, thus, effectively reduce the magnetic disorder in the septuple layers that are adjacent to the ferromagnet[73]. Fu *et al.* predicted that the monolayer CrI$_3$ couples to the nearby MnBi$_2$Te$_4$ SL through ferromagnetic interaction[73]. As a result, regardless of the MnBi$_2$Te$_4$ thickness in the middle, the sandwich system is always in the QAH phase due to the net magnetisation induced by CrI$_3$. For example, Figure 6(j) shows a heterostructure for realising QAHE at a higher temperature using this strategy where a magnetic Dirac gap of 34 meV is discovered in the 4 SL MnBi$_2$Te$_4$ sandwiched between two CrI$_3$ monolayers. Using this strategy, one can also engineer QAH phase in other heterostructures formed by MnBi$_2$Te$_4$ of different thicknesses with a monolayer of CrI$_3$, as shown in Figure 6(k). One slight problem is the Cr *3d* bands are quite close to the Dirac band gap. However, considering the highly localised nature of the *3d* bands, if the electrodes can be placed away from the CrI$_3$ layer, one should still be able to achieve chiral edge channel transport without interference from *3d* states.

Figure 6 Strategies for realising quantum anomalous Hall effect at higher temperature via heterostructure engineering. a) Schematic diagram of a sandwich heterostructure formed by a topological insulator layer sandwiched between two 2D ferromagnetic insulator layers. The green arrow implies the spin polarised chiral edge current and the inset depicts the extended wave function distribution in the direction perpendicular to the film. b-d) ARPES results on an MBT-[BT]$_{4QL}$-MBT heterostructure and calculated spin-polarised band structure. b) Energy dispersion along GM direction taken at 8 K, c) energy dispersion along GK direction taken at 8 K and d) spin-resolved energy bands from DFT calculation along GK. e) Schematics of a MnBi$_2$Te$_4$- Sb$_2$Te$_3$- MnBi$_2$Te$_4$ heterostructure. f) DFT calculated band structure (blue) and Berry curvature (red). g) Zoom-in of the band structure close to Γ point. h) Hall conductance calculated as a function of energy near Fermi level. The heterostructure has a quantised Hall conductance of e^2/h in the gap. i) Band structure of the heterostructure in a nanoribbon geometry where a chiral edge state connecting valence band and conduction band is clearly visible. j-k) DFT calculated band structures of heterostructures: CrI$_3$-[MBT]$_{4SL}$- CrI$_3$, CrI$_3$-[MBT]$_{1SL}$, CrI$_3$-[MBT]$_{2SL}$, and CrI$_3$-[MBT]$_{3SL}$. This figure is reproduced from ref.[68, 69, 73]

Conclusion and outlook

In conclusion, it is clear based on recent experimental progress using ARPES, electrical transport, magnetometry, and STM, that magnetic disorder and nonuniformity of the sample thickness remain an ongoing challenge in $MnBi_2Te_4$ MBE thin films and even exfoliated flakes. The reduced magnetic coupling in the uncompensated layer and the presence of a high concentration of magnetic defects result in Dirac gap and local doping fluctuations throughout the $MnBi_2Te_4$ MBE thin films. Consequently, dissipationless chiral edge state transport can be suppressed by mechanisms such as bulk-edge state scatting and inter-domain tunnelling processes. Nevertheless, the intrinsic magnetic order in $MnBi_2Te_4$ offers a promising pathway towards higher temperature QAHE and is more likely to succeed than dilute magnetic doped topological insulators. In the hope of overcoming these issues, we have summarized several strategies based on recent experiments and theory progress on heterostructure engineering using 2D ferromagnet, $MnBi_2Te_4$ and topological insulators of similar structures such as Bi_2Te_3 and Sb_2Te_3. These strategies offer several key advantages including a large Dirac gap, higher magnetic transition temperature, and reduced magnetic disorder because magnetic order is induced via proximity. The heterostructures host the QAH insulator phase regardless of the thickness of the middle layer, such as Bi_2Te_3 sandwiched by $MnBi_2Te_4$ and $MnBi_2Te_4$ sandwiched by CrI_3[67, 73], meaning MBE thin films that are not of perfectly uniform thickness could still be very promising.

Realizing the quantum anomalous Hall effect at room temperature with zero longitudinal resistance is still a major milestone yet to be achieved, and still an actively evolving research field. Magnetic topological insulators and their heterostructures are the most studied material systems for the QAHE, and large-size QAHE devices with a high degree of quantisation have been routinely fabricated using MBE. Nevertheless, the topological insulators discovered to date still suffer from parasitic magnetic disorder problems and highly sample-dependent device performance, possibly due to the vast presence of magnetic defects and impurity phases. The heterostructure engineering strategy summarised above is a promising solution to these problems, with versatility in material selection. Meanwhile, in addition, the research community is exploring other emergent material systems, especially intrinsic magnetic topological insulators thin films outside the magnetic tetradymite family. Two examples are Kagome metals $Co_3Sn_2S_2$ and Mn_3Sn, which are Weyl semimetals in the bulk form. The Weyl semimetal phase is intimately connected to the QAHE phase, where the Weyl nodes can be gapped out in the thin film limit and induce a QAHE phase. However, reducing the thickness to the thin film limit can be very challenging given that these Kagome materials are not van der Waals materials and possess a 3D crystal structure and bonding. Another particularly promising material system is moiré materials-based devices where the QAHE was observed at 1.6 K in a h-BN sandwiched twisted bilayer graphene device [30] and 2.5 K in AB-stacked $MoTe_2/WSe_2$ heterobilayers[31]. These QAHE devices show different behaviour from magnetic topological insulators: the magnetism originates from orbital magnetism instead of FM/AFM order. Moreover, in these devices, the Hall resistance can go over $\frac{\hbar}{e^2}$, unlike $MnBi_2Te_4$ where the Hall resistance is always smaller than $\frac{\hbar}{e^2}$ at finite longitudinal resistance, suggesting different disorder mechanisms[74]. A similar magnetic domain problem is also present in these moiré systems, possibly arising from the relaxation of lattice strain in the form of fluctuation of twist angle. In the end, engineering high-performance QAHE devices requires robust magnetism, non-trivial band topology, and homogeneous doping level throughout the sample. It is certainly critical to understand and optimise each aspect carefully. However, in the course

of searching for a robust QAHE material, it is important not to overlook the interplay between magnetism, band topology, and crystal defects. In the example of $MnBi_2Te_4$, magnetism can be affected by band structure through strong *p-d* hybridisation. On the contrary, the band structure is coupled to magnetism *via* exchange coupling. The omnipresent defects in the sample can alternate local doping levels, induce magnetic disorder, as well as lead to highly sample-dependent electronic properties.

Acknowledgements

Reference

1. M. König, S. Wiedmann, C. Brüne, A. Roth, H. Buhmann, L. W. Molenkamp, X.-L. Qi and S.-C. Zhang, *Science*, 2007, **318**, 766-770.
2. S. Wu, V. Fatemi, Q. D. Gibson, K. Watanabe, T. Taniguchi, R. J. Cava and P. Jarillo-Herrero, *Science*, 2018, **359**, 76-79.
3. C.-Z. Chang, J. Zhang, X. Feng, J. Shen, Z. Zhang, M. Guo, K. Li, Y. Ou, P. Wei, L.-L. Wang, Z.-Q. Ji, Y. Feng, S. Ji, X. Chen, J. Jia, X. Dai, Z. Fang, S.-C. Zhang, K. He, Y. Wang, L. Lu, X.-C. Ma and Q.-K. Xue, *Science*, 2013, **340**, 167-170.
4. Y. Ou, C. Liu, G. Jiang, Y. Feng, D. Zhao, W. Wu, X.-X. Wang, W. Li, C. Song, L.-L. Wang, W. Wang, W. Wu, Y. Wang, K. He, X.-C. Ma and Q.-K. Xue, *Advanced Materials*, 2018, **30**, 1703062.
5. P. Li, X. Li, W. Zhao, H. Chen, M.-X. Chen, Z.-X. Guo, J. Feng, X.-G. Gong and A. H. MacDonald, *Nano Letters*, 2017, **17**, 6195-6202.
6. K. Wang, Y. Li, H. Mei, P. Li and Z.-X. Guo, *Physical Review Materials*, 2022, **6**, 044202.
7. P. Li, X. Yang, Q.-S. Jiang, Y.-Z. Wu and W. Xun, *Physical Review Materials*, 2023, **7**, 064002.
8. B. A. Bernevig, T. L. Hughes and S.-C. Zhang, *Science*, 2006, **314**, 1757-1761.
9. R. Yu, W. Zhang, H.-J. Zhang, S.-C. Zhang, X. Dai and Z. Fang, *Science*, 2010, **329**, 61-64.
10. Y. Tokura, K. Yasuda and A. Tsukazaki, *Nature Reviews Physics*, 2019, **1**, 126-143.
11. B. Lian, X.-Q. Sun, A. Vaezi, X.-L. Qi and S.-C. Zhang, *Proceedings of the National Academy of Sciences*, 2018, **115**, 10938-10942.
12. Y. Gong, J. Guo, J. Li, K. Zhu, M. Liao, X. Liu, Q. Zhang, L. Gu, L. Tang, X. Feng, D. Zhang, W. Li, C. Song, L. Wang, P. Yu, X. Chen, Y. Wang, H. Yao, W. Duan, Y. Xu, S.-C. Zhang, X. Ma, Q.-K. Xue and K. He, *Chinese Physics Letters*, 2019, **36**, 076801.
13. Y. Deng, Y. Yu, M. Z. Shi, Z. Guo, Z. Xu, J. Wang, X. H. Chen and Y. Zhang, *Science*, 2020, **367**, 895-900.
14. Y. Bai, Y. Li, J. Luan, R. Liu, W. Song, Y. Chen, P.-F. Ji, Q. Zhang, F. Meng, B. Tong, L. Li, Y. Jiang, Z. Gao, L. Gu, J. Zhang, Y. Wang, Q.-K. Xue, K. He, Y. Feng and X. Feng, *National Science Review*, 2023, DOI: 10.1093/nsr/nwad189, nwad189.

15. Y. Zhang, K. He, C.-Z. Chang, C.-L. Song, L.-L. Wang, X. Chen, J.-F. Jia, Z. Fang, X. Dai, W.-Y. Shan, S.-Q. Shen, Q. Niu, X.-L. Qi, S.-C. Zhang, X.-C. Ma and Q.-K. Xue, *Nature Physics*, 2010, **6**, 584-588.

16. Y. Zhang, T.-R. Chang, B. Zhou, Y.-T. Cui, H. Yan, Z. Liu, F. Schmitt, J. Lee, R. Moore, Y. Chen, H. Lin, H.-T. Jeng, S.-K. Mo, Z. Hussain, A. Bansil and Z.-X. Shen, *Nature Nanotechnology*, 2014, **9**, 111-115.

17. J. L. Collins, A. Tadich, W. Wu, L. C. Gomes, J. N. B. Rodrigues, C. Liu, J. Hellerstedt, H. Ryu, S. Tang, S.-K. Mo, S. Adam, S. A. Yang, M. S. Fuhrer and M. T. Edmonds, *Nature*, 2018, **564**, 390-394.

18. F. Reis, G. Li, L. Dudy, M. Bauernfeind, S. Glass, W. Hanke, R. Thomale, J. Schäfer and R. Claessen, *Science*, 2017, **357**, 287-290.

19. Y. Yuan, X. Wang, H. Li, J. Li, Y. Ji, Z. Hao, Y. Wu, K. He, Y. Wang, Y. Xu, W. Duan, W. Li and Q.-K. Xue, *Nano Letters*, 2020, **20**, 3271-3277.

20. M. Garnica, M. M. Otrokov, P. C. Aguilar, I. I. Klimovskikh, D. Estyunin, Z. S. Aliev, I. R. Amiraslanov, N. A. Abdullayev, V. N. Zverev, M. B. Babanly, N. T. Mamedov, A. M. Shikin, A. Arnau, A. L. V. de Parga, E. V. Chulkov and R. Miranda, *npj Quantum Materials*, 2022, **7**, 7.

21. Z. Huang, M.-H. Du, J. Yan and W. Wu, *Physical Review Materials*, 2020, **4**, 121202.

22. G. Akhgar, Q. Li, I. Di Bernardo, C. X. Trang, C. Liu, A. Zavabeti, J. Karel, A. Tadich, M. S. Fuhrer and M. T. Edmonds, *ACS Applied Materials & Interfaces*, 2022, **14**, 6102-6108.

23. A. R. Mazza, J. Lapano, H. M. MeyerIii, C. T. Nelson, T. Smith, Y.-Y. Pai, K. Noordhoek, B. J. Lawrie, T. R. Charlton, R. G. Moore, T. Z. Ward, M.-H. Du, G. Eres and M. Brahlek, *Advanced Functional Materials*, 2022, **32**, 2202234.

24. F. D. M. Haldane, *Physical Review Letters*, 1988, **61**, 2015-2018.

25. G. Jotzu, M. Messer, R. Desbuquois, M. Lebrat, T. Uehlinger, D. Greif and T. Esslinger, *Nature*, 2014, **515**, 237-240.

26. X.-L. Qi, Y.-S. Wu and S.-C. Zhang, *Physical Review B*, 2006, **74**, 085308.

27. X. Feng, Y. Feng, J. Wang, Y. Ou, Z. Hao, C. Liu, Z. Zhang, L. Zhang, C. Lin, J. Liao, Y. Li, L.-L. Wang, S.-H. Ji, X. Chen, X. Ma, S.-C. Zhang, Y. Wang, K. He and Q.-K. Xue, *Advanced Materials*, 2016, **28**, 6386-6390.

28. A. J. Bestwick, E. J. Fox, X. Kou, L. Pan, K. L. Wang and D. Goldhaber-Gordon, *Physical Review Letters*, 2015, **114**, 187201.

29. C.-Z. Chang, W. Zhao, D. Y. Kim, H. Zhang, B. A. Assaf, D. Heiman, S.-C. Zhang, C. Liu, M. H. W. Chan and J. S. Moodera, *Nature Materials*, 2015, **14**, 473-477.

30. M. Serlin, C. L. Tschirhart, H. Polshyn, Y. Zhang, J. Zhu, K. Watanabe, T. Taniguchi, L. Balents and A. F. Young, *Science*, 2020, **367**, 900-903.

31. T. Li, S. Jiang, B. Shen, Y. Zhang, L. Li, Z. Tao, T. Devakul, K. Watanabe, T. Taniguchi, L. Fu, J. Shan and K. F. Mak, *Nature*, 2021, **600**, 641-646.

32. D. F. Liu, A. J. Liang, E. K. Liu, Q. N. Xu, Y. W. Li, C. Chen, D. Pei, W. J. Shi, S. K. Mo, P. Dudin, T. Kim, C. Cacho, G. Li, Y. Sun, L. X. Yang, Z. K. Liu, S. S. P. Parkin, C. Felser and Y. L. Chen, *Science*, 2019, **365**, 1282-1285.

33. K. Kuroda, T. Tomita, M. T. Suzuki, C. Bareille, A. A. Nugroho, P. Goswami, M. Ochi, M. Ikhlas, M. Nakayama, S. Akebi, R. Noguchi, R. Ishii, N. Inami, K. Ono, H. Kumigashira, A. Varykhalov, T. Muro, T. Koretsune, R. Arita, S. Shin, T. Kondo and S. Nakatsuji, *Nature Materials*, 2017, **16**, 1090-1095.

34. P. Li, *Physical Chemistry Chemical Physics*, 2019, **21**, 6712-6717.

35. C. Huang, J. Zhou, H. Wu, K. Deng, P. Jena and E. Kan, *Physical Review B*, 2017, **95**, 045113.
36. Z. F. Wang, Z. Liu and F. Liu, *Physical Review Letters*, 2013, **110**, 196801.
37. Y. Deng, Y. Yu, M. Z. Shi, Z. Guo, Z. Xu, J. Wang, X. H. Chen and Y. Zhang, *Science*, 2020, **367**, 895-900.
38. W. Lin, Y. Feng, Y. Wang, J. Zhu, Z. Lian, H. Zhang, H. Li, Y. Wu, C. Liu, Y. Wang, J. Zhang, Y. Wang, C.-Z. Chen, X. Zhou and J. Shen, *Nature Communications*, 2022, **13**, 7714.
39. S. Yang, X. Xu, Y. Zhu, R. Niu, C. Xu, Y. Peng, X. Cheng, X. Jia, Y. Huang, X. Xu, J. Lu and Y. Ye, *Physical Review X*, 2021, **11**, 011003.
40. I. Lee, C. K. Kim, J. Lee, S. J. L. Billinge, R. Zhong, J. A. Schneeloch, T. Liu, T. Valla, J. M. Tranquada, G. Gu and J. C. S. Davis, *Proceedings of the National Academy of Sciences*, 2015, **112**, 1316-1321.
41. K. M. Fijalkowski, N. Liu, P. Mandal, S. Schreyeck, K. Brunner, C. Gould and L. W. Molenkamp, *Nature Communications*, 2021, **12**, 5599.
42. M. Mogi, R. Yoshimi, A. Tsukazaki, K. Yasuda, Y. Kozuka, K. S. Takahashi, M. Kawasaki and Y. Tokura, *Applied Physics Letters*, 2015, **107**, 182401.
43. M. M. Otrokov, I. P. Rusinov, M. Blanco-Rey, M. Hoffmann, A. Y. Vyazovskaya, S. V. Eremeev, A. Ernst, P. M. Echenique, A. Arnau and E. V. Chulkov, *Physical Review Letters*, 2019, **122**, 107202.
44. J. Li, Y. Li, S. Du, Z. Wang, B.-L. Gu, S.-C. Zhang, K. He, W. Duan and Y. Xu, *Science Advances*, 2019, **5**, eaaw5685.
45. B. Li, J. Q. Yan, D. M. Pajerowski, E. Gordon, A. M. Nedić, Y. Sizyuk, L. Ke, P. P. Orth, D. Vaknin and R. J. McQueeney, *Physical Review Letters*, 2020, **124**, 167204.
46. C. X. Trang, Q. Li, Y. Yin, J. Hwang, G. Akhgar, I. Di Bernardo, A. Grubišić-Čabo, A. Tadich, M. S. Fuhrer, S.-K. Mo, N. V. Medhekar and M. T. Edmonds, *ACS Nano*, 2021, **15**, 13444-13452.
47. Y. Gong, J. Guo, J. Li, K. Zhu, M. Liao, X. Liu, Q. Zhang, L. Gu, L. Tang, X. Feng, D. Zhang, W. Li, C. Song, L. Wang, P. Yu, X. Chen, Y. Wang, H. Yao, W. Duan, Y. Xu, S.-C. Zhang, X. Ma, Q.-K. Xue and K. He, *Chinese Physics Letters*, 2019, **36**, 076801.
48. J. Luo, Q. Tong, Z. Jiang, H. Bai, J. Wu, X. Liu, S. Xie, H. Ge, Y. Zhao, Y. Liu, M. Hong, D. Shen, Q. Zhang, W. Liu and X. Tang, *ACS Nano*, 2023, **17**, 19022-19032.
49. S.-H. Su, J.-T. Chang, P.-Y. Chuang, M.-C. Tsai, Y.-W. Peng, M. K. Lee, C.-M. Cheng and J.-C. A. Huang, *Journal*, 2021, **11**.
50. F. Lüpke, A. D. Pham, Y.-F. Zhao, L.-J. Zhou, W. Lu, E. Briggs, J. Bernholc, M. Kolmer, J. Teeter, W. Ko, C.-Z. Chang, P. Ganesh and A.-P. Li, *Physical Review B*, 2022, **105**, 035423.
51. M. Liu, C. Lei, H. Kim, Y. Li, L. Frammolino, J. Yan, A. H. Macdonald and C.-K. Shih, *Proceedings of the National Academy of Sciences*, 2022, **119**, e2207681119.
52. R. Xu, Y. Bai, J. Zhou, J. Li, X. Gu, N. Qin, Z. Yin, X. Du, Q. Zhang, W. Zhao, Y. Li, Y. Wu, C. Ding, L. Wang, A. Liang, Z. Liu, Y. Xu, X. Feng, K. He, Y. Chen and L. Yang, *Nano Letters*, 2022, **22**, 6320-6327.
53. Y.-F. Zhao, L.-J. Zhou, F. Wang, G. Wang, T. Song, D. Ovchinnikov, H. Yi, R. Mei, K. Wang, M. H. W. Chan, C.-X. Liu, X. Xu and C.-Z. Chang, *Nano Letters*, 2021, **21**, 7691-7698.

54. Q. Li, I. Di Bernardo, J. Maniatis, D. McEwen, A. Dominguez-Celorrio, M. T. H. Bhuiyan, M. Zhao, A. Tadich, L. Watson, B. Lowe, T.-H.-Y. Vu, C. X. Trang, J. Hwang, S.-K. Mo, M. S. Fuhrer and M. T. Edmonds, *Advanced Materials*, 2024, **n/a**, 2312004.

55. H. Wang and X. Qian, *npj Computational Materials*, 2020, **6**, 199.

56. M. M. Otrokov, I. I. Klimovskikh, H. Bentmann, D. Estyunin, A. Zeugner, Z. S. Aliev, S. Gaß, A. U. B. Wolter, A. V. Koroleva, A. M. Shikin, M. Blanco-Rey, M. Hoffmann, I. P. Rusinov, A. Y. Vyazovskaya, S. V. Eremeev, Y. M. Koroteev, V. M. Kuznetsov, F. Freyse, J. Sánchez-Barriga, I. R. Amiraslanov, M. B. Babanly, N. T. Mamedov, N. A. Abdullayev, V. N. Zverev, A. Alfonsov, V. Kataev, B. Büchner, E. F. Schwier, S. Kumar, A. Kimura, L. Petaccia, G. Di Santo, R. C. Vidal, S. Schatz, K. Kißner, M. Ünzelmann, C. H. Min, S. Moser, T. R. F. Peixoto, F. Reinert, A. Ernst, P. M. Echenique, A. Isaeva and E. V. Chulkov, *Nature*, 2019, **576**, 416-422.

57. E. D. L. Rienks, S. Wimmer, J. Sánchez-Barriga, O. Caha, P. S. Mandal, J. Růžička, A. Ney, H. Steiner, V. V. Volobuev, H. Groiss, M. Albu, G. Kothleitner, J. Michalička, S. A. Khan, J. Minár, H. Ebert, G. Bauer, F. Freyse, A. Varykhalov, O. Rader and G. Springholz, *Nature*, 2019, **576**, 423-428.

58. Y. Bai, Y. Li, J. Luan, R. Liu, W. Song, Y. Chen, P.-F. Ji, Q. Zhang, F. Meng and B. Tong, *arXiv preprint arXiv:2206.03773*, 2022.

59. D. Ovchinnikov, X. Huang, Z. Lin, Z. Fei, J. Cai, T. Song, M. He, Q. Jiang, C. Wang, H. Li, Y. Wang, Y. Wu, D. Xiao, J.-H. Chu, J. Yan, C.-Z. Chang, Y.-T. Cui and X. Xu, *Nano Letters*, 2021, **21**, 2544-2550.

60. Y. Shi, J. Kahn, B. Niu, Z. Fei, B. Sun, X. Cai, B. A. Francisco, D. Wu, Z.-X. Shen, X. Xu, D. H. Cobden and Y.-T. Cui, *Science Advances*, **5**, eaat8799.

61. L. Peng, Y. Yuan, G. Li, X. Yang, J.-J. Xian, C.-J. Yi, Y.-G. Shi and Y.-S. Fu, *Nature Communications*, 2017, **8**, 659.

62. P. M. Sass, J. Kim, D. Vanderbilt, J. Yan and W. Wu, *Physical Review Letters*, 2020, **125**, 037201.

63. B. Li, J. Q. Yan, D. M. Pajerowski, E. Gordon, A. M. Nedić, Y. Sizyuk, L. Ke, P. P. Orth, D. Vaknin and R. J. McQueeney, *Physical Review Letters*, 2020, **124**, 167204.

64. H. Padmanabhan, V. A. Stoica, P. K. Kim, M. Poore, T. Yang, X. Shen, A. H. Reid, M.-F. Lin, S. Park, J. Yang, H. Wang, N. Z. Koocher, D. Puggioni, A. B. Georgescu, L. Min, S. H. Lee, Z. Mao, J. M. Rondinelli, A. M. Lindenberg, L.-Q. Chen, X. Wang, R. D. Averitt, J. W. Freeland and V. Gopalan, *Advanced Materials*, 2022, **34**, 2202841.

65. L. Pan, A. Grutter, P. Zhang, X. Che, T. Nozaki, A. Stern, M. Street, B. Zhang, B. Casas, Q. L. He, E. S. Choi, S. M. Disseler, D. A. Gilbert, G. Yin, Q. Shao, P. Deng, Y. Wu, X. Liu, X. Kou, S. Masashi, X. Han, C. Binek, S. Chambers, J. Xia and K. L. Wang, *Advanced Materials*, 2020, **32**, 2001460.

66. R. Watanabe, R. Yoshimi, M. Kawamura, M. Mogi, A. Tsukazaki, X. Z. Yu, K. Nakajima, K. S. Takahashi, M. Kawasaki and Y. Tokura, *Applied Physics Letters*, 2019, **115**, 102403.

67. M. M. Otrokov, T. V. Menshchikova, M. G. Vergniory, I. P. Rusinov, A. Yu Vyazovskaya, Y. M. Koroteev, G. Bihlmayer, A. Ernst, P. M. Echenique, A. Arnau and E. V. Chulkov, *2D Materials*, 2017, **4**, 025082.

68. Q. Li, C. X. Trang, W. Wu, J. Hwang, D. Cortie, N. Medhekar, S.-K. Mo, S. A. Yang and M. T. Edmonds, *Advanced Materials*, 2022, **34**, 2107520.

69. S. Qi, R. Gao, M. Chang, Y. Han and Z. Qiao, *Physical Review B*, 2020, **101**, 014423.

70. W. Zhao, Z. Fei, T. Song, H. K. Choi, T. Palomaki, B. Sun, P. Malinowski, M. A. McGuire, J.-H. Chu, X. Xu and D. H. Cobden, *Nature Materials*, 2020, **19**, 503-507.
71. S. Kezilebieke, M. N. Huda, V. Vaňo, M. Aapro, S. C. Ganguli, O. J. Silveira, S. Głodzik, A. S. Foster, T. Ojanen and P. Liljeroth, *Nature*, 2020, **588**, 424-428.
72. B. Huang, G. Clark, E. Navarro-Moratalla, D. R. Klein, R. Cheng, K. L. Seyler, D. Zhong, E. Schmidgall, M. A. McGuire, D. H. Cobden, W. Yao, D. Xiao, P. Jarillo-Herrero and X. Xu, *Nature*, 2017, **546**, 270-273.
73. H. Fu, C.-X. Liu and B. Yan, *Science Advances*, 2020, **6**, eaaz0948.
74. C.-Z. Chang, C.-X. Liu and A. H. MacDonald, *Reviews of Modern Physics*, 2023, **95**, 011002.